Journal of Materials Chemistry A

PAPER

Published on 25 June 2026

Check for updates

Cite this: DOI: 10.1039/d6ta01464j

Hybrid zirconium phosphate phosphonates as efficient hosts for confined Ni–Fe oxygen evolution catalysts

Anna Donnadio, [*a] Iolanda D'Ambrosio,[b] Gabriel Menendez Rodriguez, [bc] Ferdinando Costantino, [b] Riccardo Vivani, [a] Stefano Giovagnoli,[a] Alceo Macchioni, [bc] Beatrice Muzzi,[d] Enrique Rodríguez-Castellón [e] and Morena Nocchetti [*a]

The rational design of earth-abundant electrocatalysts for the oxygen evolution reaction (OER) requires materials platforms capable of stabilizing catalytically active species under strongly alkaline conditions while maintaining efficient charge-transfer pathways. Here, we report a family of amino acid-derived zirconium phosphate–phosphonate hybrid materials that act as structurally tunable layered hosts for the confinement of Ni^{2+} and Fe^{3+} ions. Amino acid functionalization promotes exfoliation of the layered framework into colloidal nanosheets, enabling homogeneous metal dispersion within well-defined organic–inorganic interfaces. Systematic variation of the ligand structure and Ni/Fe composition reveals clear correlations between supramolecular organization, interfacial metal coordination, and electrocatalytic performance. The glycine-derived material (ZGLY) with an optimized Ni/Fe ratio achieves an overpotential of 304 mV to reach a geometric current density of 10 mA cm^{-2} and a Tafel slope of 32.9 mV dec^{-1}, together with sustained stability in alkaline media, exhibiting enhanced activity and overall performance compared to previously reported zirconium phosphate-based OER systems. Post-*operando* Raman spectroscopy and XPS unambiguously identify NiOOH and FeOOH formed *in situ* as catalytically active phases, while XRD and electron microscopy confirm that the ZPAC scaffold preserves its structural integrity throughout the operation. These observations indicate that the ZPAC framework primarily acts as a chemically robust host, enabling the stabilization and spatial confinement of the catalytically active Ni–Fe oxyhydroxide species formed under operating conditions. Consequently, these findings highlight zirconium phosphate–phosphonates as versatile 2D hybrid materials, in which the chemical composition, interlayer organization, and metal confinement can be tuned to regulate catalytic behavior, providing new insights into the design of durable, earth-abundant water oxidation catalysts.

Received 16th February 2026
Accepted 24th June 2026

DOI: 10.1039/d6ta01464j

rsc.li/materials-a

1. Introduction

Increasing global energy demand, the depletion of fossil fuels, and their negative environmental impact are driving research into clean and sustainable energy technologies. As an alternative to fossil fuels, hydrogen (H_2) is considered a promising energy vector,[1] particularly when produced *via* direct electrochemical water splitting, which offers a sustainable and cost-effective pathway.[2] However, reducing the energy consumption of water electrolysis remains a key challenge for the large-scale deployment of "green" hydrogen. Water electrolysis involves two half reactions: the cathodic hydrogen evolution reaction (HER) and the anodic oxygen evolution reaction (OER). The HER is a relatively simple two-electron transfer process involving electrochemical H^+ adsorption and desorption of H_2. Conversely, the OER is a more complex process with sluggish oxygen evolution kinetics that makes it the limiting half-reaction. In the OER, four electrons and four protons have to be transferred in a multi-step reaction, each of which produces the formation of an intermediate. The formation of these intermediates introduces significant energy barriers, making the OER the rate-limiting step and the primary contributor to the overpotential in water electrolysis.[3,4] Because of this, the rational design of catalysts capable of promoting the OER by reducing its overpotential is a key step toward the realization of a widely applicable power-to-fuel scheme *via* water electrolysis. Until now, heterogeneous

[a] *Department of Pharmaceutical Sciences, University of Perugia, Via del Liceo 1, 06123 Perugia, Italy. E-mail: anna.donnadio@unipg.it; morena.nocchetti@unipg.it*

[b] *Department of Chemistry, Biology and Biotechnologies, University of Perugia, Via del Liceo 1, 06123 Perugia, Italy*

[c] *CIRCC, Interuniversity Consortium for Chemical Reactivity and Catalysis, Via C. Ulpiani, 27, 70 126 Bari, Italy*

[d] *Institute of Chemistry of Organometallic Compounds – CNR, Via Madonna del Piano 10, 50019 Sesto Fiorentino, FI, Italy*

[e] *Department of Inorganic Chemistry, Institute for Interuniversity Research in Bio-Refineries (I3B), Faculty of Sciences, University of Málaga, 29071 Málaga, Spain*

catalysts based on transition metals have been widely investigated because of their outstanding OER catalytic activity. Noble-metal oxides such as RuO_2 and IrO_2 remain benchmark OER catalysts.[5,6] However, their high cost, limited availability, and poor stability in strongly alkaline media restrict large-scale applications. These limitations have driven significant interest in low-cost, earth-abundant alternatives, particularly first-row transition metals.[7] OER electrocatalysts based on Fe, Co, and Ni, in the form of oxides and (oxy)hydroxides, layered double hydroxides,[8,9] MXenes,[10] phosphates, dichalcogenides, nitrides, borides and carbides, have shown very high performance.[5] Interestingly, it has been observed that during the OER, these catalysts transform into other oxide phases, generally metal (oxy) hydroxides, which perform better than the parent material.[11] The formation of these active phases in a confined environment, such as two-dimensional (2D) materials, is a recently proposed strategy to stabilise them, avoiding aggregation and making the active sites available. Among 2D materials, transition metal dichalcogenides,[12,13] layered (oxy)hydroxides,[14] graphene[15] and zirconium phosphate (ZrP) have been investigated.[16] The ion-exchange capability and electrochemical stability of ZrP make it an effective support for transition metal-based OER catalysts in alkaline media.[17] α-ZrP with intercalated or adsorbed Fe^{2+}, Fe^{3+}, Co^{2+}, and Ni^{2+} ions showed interesting catalytic activity for the OER, requiring overpotentials of 0.5–0.7 V to achieve a current density of 10 mA cm^{-2}. The catalytic performance of layered ZrP materials improves upon exfoliation, as the OER predominantly occurs on the outer surfaces of the nanoparticles.[18] Moreover, the loading and coverage of cobalt and nickel on ZrP with different morphologies also affect the OER activity.[19] More recently, the confinement of nickel-iron mixtures in the interlayer environment of the ZrP layered structure has been found to stabilize Fe-rich compositions. The enhanced activity and stability of the resulting OER catalysts were primarily attributed to the species intercalated within the layers, rather than to those adsorbed on the surface.[16] The synthesis of zirconium phosphonates from phosphonic acids bearing amino acid functionalities has led to materials with structural arrangements and reactivity markedly different from those of conventional α- and γ-type zirconium phosphonates.[20] In particular, zirconium phosphate phosphonates derived from *N*,*N*-bis(phosphonomethyl)aminocarboxylic acids with branched structures, synthesized from glycine, 4-aminobutyric acid, 5-aminovaleric acid, and 6-aminocaproic acid, exhibit unique coordinative and exfoliation properties. These zirconium phosphate bis(phosphonomethyl)aminocarboxylates (ZPACs) display efficient interactions with cations and basic molecules due to the presence of exposed –COOH and P–OH groups on the layer surfaces.[21,22] Palladium and silver NPs were efficiently immobilized on ZPACs to obtain catalysts[23–25] and antibacterial materials.[22,26]

Despite the growing interest in layered zirconium phosphate derivatives as hosts for transition metal species, their potential as chemically tunable hybrid platforms for stabilizing earth-abundant OER catalysts remains underexplored. In particular, the influence of organic phosphonate functionalization, interlayer organization, and exfoliation degree on metal coordination and catalytic response has not been systematically investigated. In this paper, the coordination ability of ZPACs was exploited to immobilize Fe^{3+} and Ni^{2+} ions on previously exfoliated materials in order to prepare efficient and stable electrocatalysts for the OER in alkaline media. The presence of exposed functional groups on the surfaces of the exfoliated ZPAC layers enabled strong interactions with Ni and Fe ions, promoting homogeneous dispersion and preventing aggregation of the active species. The structural flexibility, high ion-exchange capacity, and excellent dispersion characteristics of the exfoliated ZPAC materials allowed for the fine-tuning of the metal loading and the local coordination environment. These features contributed to increasing the electrochemically active surface area, improving the electron transfer kinetics, and enhancing the catalytic efficiency. By leveraging the unique structural and chemical properties of exfoliated ZPAC materials, we provided a promising route for the development of next-generation OER catalysts based on earth-abundant transition metals, with potential implications for sustainable hydrogen production and energy conversion technologies.

2. Experimental section

2.1 Materials

Zirconium oxychloride octahydrate ($ZrOCl_2 \cdot 8H_2O$, 98%) was obtained from Alfa Aesar. Multi-walled carbon nanotubes, iron(III) chloride ($FeCl_3$), nickel(II) acetate tetrahydrate ($Ni(OCOCH_3)_2 \cdot 4H_2O$, 98%), Nafion™ 1100 perfluorinated resin solution (5 wt%) and all other chemicals were purchased from Merck and used as received without any further purification.

2.2 Synthesis of zirconium phosphate bis(phosphonomethyl)aminocarboxylates

The *N*,*N*-bis(phosphonomethyl)aminocarboxylic acids with the formula $(H_2O_3PCH_2)_2N(CH_2)_nCOOH$, with n = 1, 3, 4, and 5 (hereafter denoted as H_5L) were synthesized by the Moedritzer–Irani reaction[27] starting from the corresponding amino acids (glycine for $n = 1$, 4-aminobutyric acid for $n = 3$, 5-aminovaleric acid for $n = 4$, and 6-aminocaproic acid for $n = 5$), as reported in ref. 22. The synthesis of the corresponding zirconium phosphate bis(phosphonomethyl)aminocarboxylates with the formula $Zr_2(PO_4)H_5[(O_3PCH_2)_2N(CH_2)_nCOO]_2 \cdot mH_2O$ (hereafter denoted as ZGLY for n = 1; ZGABA for n = 3; ZVAL for n = 4; ZCAP for $n = 5$; ZPAC in general) has been carried out following the method reported in ref. 21 and 22. Briefly, 9 mmol of H_5L were solubilized in 93 mL of a suitable solvent (water for ZGLY and ZGABA; 1 : 9 V/V propanol–water for ZVAL; 1 : 1 V/V propanol–water for ZCAP) and 6 mL of 1 M H_3PO_4 was added to this solution (H_5L/H_3PO_4 molar ratio = 1.5). A second solution was obtained by dissolving 1.93 g $ZrOCl_2 \cdot 8H_2O$ (5.9 mmol) in 20.4 mL of 2.9 M HF (59 mmol; HF/Zr^{4+} molar ratio = 10). These solutions were mixed in a 500 mL Teflon bottle and put in an oven for three days at 90 °C. Then, the product was filtered and washed three times with water and dried in an oven at 60 °C. The calculated ion exchange capacity (IEC) for ZGLY, ZGABA, ZVAL and ZCAP is 3.8, 3.5, 3.4, and 3.3 mequiv per g, respectively.

2.3 Preparation of NiFeZPAC catalysts

The metal-ZPACs, in the form of colloidal dispersions, were obtained after the exfoliation of ZPACs followed by direct ion exchange. First, 100 mg of ZPACs were suspended in 20 mL of water, and 0.1 M *n*-propylamine was added dropwise (1.2 mL for ZGLY; 1.1 mL for ZGABA; 1.0 mL for ZVAL; 1 mL for ZCAP; ZPAC/*n*-propylamine molar ratio of 1.1) under vigorous magnetic stirring. This mixture was stirred for at least one hour, up to complete exfoliation and the formation of a stable colloidal dispersion of lamellae. To the ZGLY dispersion, volumes of 0.05 M $Ni(CH_3COO)_2 \cdot 4H_2O$ and 0.05 M $FeCl_3$, previously mixed, were added dropwise in order to achieve the following Ni molar fractions (x_{Ni} = Ni(II)/(Ni(II) + Fe(III))): 1, 0.85, 0.75, 0.25 and 0.10. As far as ZGABA, ZVAL, and ZCAP dispersions, they were treated with a solution containing an x_{Ni} equal to 0.75. After 24 hours under stirring, the products were recovered by centrifugation and washed three times with deionized water and resuspended in 20 mL of deionized water. A known volume of each functionalized dispersion was dried to constant weight in an oven at 100 °C to determine the content of anhydrous metal-ZPAC in the dispersions. The content of metal-ZPAC in each dispersion was found to be 4 mg mL^{-1}.

To determine the metal uptake, a fraction of the dispersion was recovered by centrifugation (5000 rpm for 15 min), dried in an oven at 100 °C, and analyzed by ICP upon acid digestion. The amount of salt solutions used is reported in Table 1 beside the amount of metal uptake expressed as x_{Ni} in the solid.

2.4 Material characterization

The amounts of iron, nickel, zirconium and phosphorus were obtained by inductively coupled plasma-optical emission spectrophotometry (ICP-OES) using a Varian Liberty Series II instrument working in axial geometry after the mineralization of samples with hydrofluoric acid and nitric acid. Field emission-scanning electron microscopy (FE-SEM) images were collected with a LEO 1525 ZEISS instrument working with an acceleration voltage of 15 kV. The elemental mapping of metals in samples was performed by using energy-dispersive X-ray spectroscopy (EDS). X-ray diffraction (XRD) patterns were collected with Cu-Kα radiation on a Bruker D8 Advance diffractometer and PW3050 goniometer, equipped with a Lynxeye XE-T detector. The long fine focus (LFF) ceramic tube was operated at 40 kV and 40 mA.

Attenuated total reflection (ATR) measurements were carried out with a Shimadzu IR-8000 spectrophotometer. The spectral range collected was 400 to 4000 cm^{-1}, with a spectral resolution of 4 cm^{-1}, acquiring 200 scans.

Raman spectra were acquired by using a WITec Raman Alpha300RA confocal microscope (WITec, Ulm, Germany) equipped with a 532 nm excitation wavelength and a 75 mW diode pump solid state laser. Samples deposited on FTO were directly placed on a microscopy glass specimen at room temperature. Spectra were acquired by accumulation of 80 scans at 1 s integration time in the Stokes range of 0–3600 cm^{-1}. Spectra were processed by shape baseline subtraction at 150 size and cosmic ray removal. 2D scans were performed on a 60 × 60 μm area at 100 × 100 pixel resolution and 30 mW laser power, using a Zeiss EC Epiplan-Neofluar Dic 100×/0.9 objective. All scans and spectra were processed using WITec Suite 7.0 software.

Scanning transmission electron microscopy (STEM), high-angle annular dark field (HAADF) and bright field (BF) images were acquired using a TALOS F200X G2 (Thermo Fisher Scientific). This microscope is equipped with a high-brightness field emission gun (X-FEG, 80–200 keV) and four in-column SDD Super-X detectors for energy-dispersive X-ray spectroscopy (EDS), which was used to determine the distribution of nickel and iron ions on ZPACs.

X-ray photoelectron spectroscopy (XPS) analyses were performed using a Physical Electronics VersaProbe II spectrometer equipped with a monochromatic Al Kα X-ray source ($h\nu = 1486.6$ eV). Charge compensation was achieved using a dual-beam charge neutralizer operating at 100 W and 20 kV. All measurements were conducted under ultra-high vacuum conditions ($\approx 10^{-7}$ Pa). The acquired spectra were fitted using PHI SmartSoft software and further processed with the MultiPak package (version 9.3). Binding energy calibration was carried out by referencing the C 1s peak of adventitious carbon to 284.8 eV, which was also used to correct for any charging-induced shifts.

2.5 Electrochemical measurements

Electrochemical studies were performed using a Squidstat Solo potentiostat (Admiral Instruments) in a three-electrode

Table 1 Volumes of 0.05 M $Ni(OCOCH_3)_2 \cdot 4H_2O$ and 0.05 M $FeCl_3$ used to prepare the NiFeZPAC catalysts, x_{Ni} in solution and in the solid as determined with ICP

	Ni^{2+} (mL)	Fe^{3+} (mL)	Ni/(Fe + Ni) solution molar fraction	Ni/(Fe + Ni) solid molar fraction
NiZGLY	2.0	—	1	1
$Ni_{0.89}Fe_{0.11}$ZGLY	2.8	0.5	0.85	0.89
$Ni_{0.68}Fe_{0.32}$ZGLY	2.4	0.8	0.75	0.68
$Ni_{0.48}Fe_{0.52}$ZGLY	0.66	1.96	0.25	0.48
$Ni_{0.40}Fe_{0.60}$ZGLY	0.25	2.24	0.10	0.40
$Ni_{0.79}Fe_{0.21}$ZGABA	2.4	0.78	0.75	0.79
$Ni_{0.78}Fe_{0.22}$ZVAL	2.2	0.78	0.74	0.78
$Ni_{0.77}Fe_{0.23}$ZCAP	2.2	0.74	0.75	0.77

configuration, employing a 3 mm diameter glassy carbon disk or a FTO as the working electrode, a platinum wire as the counter electrode, and a Hg/HgO (1 M NaOH) reference electrode. All measurements were carried out at room temperature using a 0.1 M KOH solution as electrolyte. All polarization curves were corrected for ohmic losses (*iR*-correction) using the solution resistance extracted from the high-frequency intercept of electrochemical impedance spectroscopy measurements.

Before use, the Hg/HgO electrode was calibrated against the reversible hydrogen electrode (RHE) by measuring the open-circuit potential (OCP) between a Pt/H_2 working electrode and the Hg/HgO reference electrode. Both electrodes were immersed in a 0.1 M KOH solution and the OCP was recorded over 10 minutes. This procedure was repeated three times, yielding an average value of 0.888 V. Accordingly, all potentials reported in this study are referenced to the reversible hydrogen electrode (RHE) using the equation E (V *vs.* RHE) = E (V *vs.* Hg/HgO) + 0.888 V.[7] Cyclic voltammograms (CVs) were recorded with scan rates of 20 and 100 mV s^{-1}, whereas the linear sweep voltammetry (LSV) curves were recorded from 1.388 to 1.688 V with a scan rate of 5 mV s^{-1}. The good operational stability over repeated cycling of ZPACs was assessed by evaluating the current decrease at 1.888 V *vs.* RHE after 100 cycles from 0.888 to 1.888 V at 100 mV s^{-1}. Chronoamperometric measurements were performed using an FTO as the working electrode, a Pt wire counter electrode, and a Hg/HgO reference electrode in 0.1 M KOH. In a first set of experiments, a potential of 1.568 V was applied for 3 h (sampling interval: 5 s) to all four NiFeZPAC catalysts, serving as a preliminary stability screen across the series. Subsequently, a long-term stability test for 24 h was performed on the best-performing catalyst, applying the same potential and sampling conditions under continuous OER operation. The electrochemically active surface area (ECSA) was calculated using the fitted value of the double layer capacitance (C_{dl}) by using the formula ECSA = C_{dl}/C_s, in which C_s is the specific capacitance of the electrolyte, which was set to a value of 40 μF cm^{-2}.[28] C_{dl} was determined by recording CVs at different scan rates (5–800 mV s^{-1}) in a non-faradaic region and corresponds to one-half of the slope of the linear fit of the capacitive current ($\Delta_i = i_a - i_c$) *versus* scan rate plot, where i_a and i_c represent the anodic and cathodic currents, respectively, measured at the same potential in the non-faradaic region of the cyclic voltammogram (Fig. S7–S10). The values of turnover frequency (TOF) were calculated by assuming that every active metal atom is involved in the catalysis (lower TOF limits were calculated): TOF = $I/(4 \times F \times n)$, where I is the measured current at a certain overpotential, the number 4 means 4 electrons per mole of O_2, F is Faraday's constant (96 500 C mol^{-1}) and n is the number of moles of the total active metals on the substrate.[29] The Nyquist plots were acquired from electrochemical impedance spectroscopy (EIS) measurements over a scanning frequency range of 100 kHz to 0.1 Hz at 0.01 V.

The electrocatalyst ink was prepared by mixing 500 μL of metal-ZPAC dispersion (4 mg mL^{-1}), 1.5 mL of isopropanol, 1 mg of carbon nanotubes (CNTs) and 10 μL of Nafion as a binder. The dispersion was sonicated for 30 minutes to obtain a homogeneous ink. For LSV and CV measurements, 10 μL of the resulting suspension was added dropwise onto the surface of a glassy carbon electrode and dried in air until the solvent evaporated. The catalyst concentration in the ink was 1 mg mL^{-1}, corresponding to a catalyst loading of approximately 0.14 mg cm^{-2} on the electrode surface (geometric area of 0.0707 cm^2). For XRD, Raman and XPS analyses performed on ink samples before and after electrocatalytic tests, the working electrode was prepared by drop-casting 10 μL of the catalyst ink onto FTO, followed by air drying.

3. Results and discussion

3.1 Synthesis and characterization of NiFeZPAC catalysts

ZPACs were synthesized by slow decomposition of Zr(IV) fluoro complexes in the presence of H_5L and phosphoric acid. All materials exhibited P/Zr and L/PO_4 molar ratios close to 2.5 and 2, respectively, consistent with the general formula $Zr_2(PO_4)H_5(L)_2 \cdot mH_2O$. Detailed crystallographic data for ZGLY, ZGABA and ZVAL have already been reported in ref. 21 and 22 with the complete structural description. Here, the schematic structure of anhydrous ZGLY, as a representative member of ZPAC isoreticular compounds, is reported in Fig. 1. The layer of ZPAC consists of two planes of Zr octahedra connected by tetradentate phosphate groups located in the inner part of the layer. The two O_3PC phosphonate tetrahedra of the phosphonic acid complete the coordination of Zr in the outer part of the layer. The two phosphonate tetrahedra are not chemically equivalent; one is tridentate and the other is monodentate with a free OH group. In this arrangement, the aminocarboxylic tails face the interlayer region. In this way, acid groups such as –COOH and –POH are exposed on the surface. This results in a high ability to intercalate basic molecules *via* acid–base reactions and to exchange protons with metal cations. Furthermore, the intercalation of propylamine produces a rapid swelling of the layered

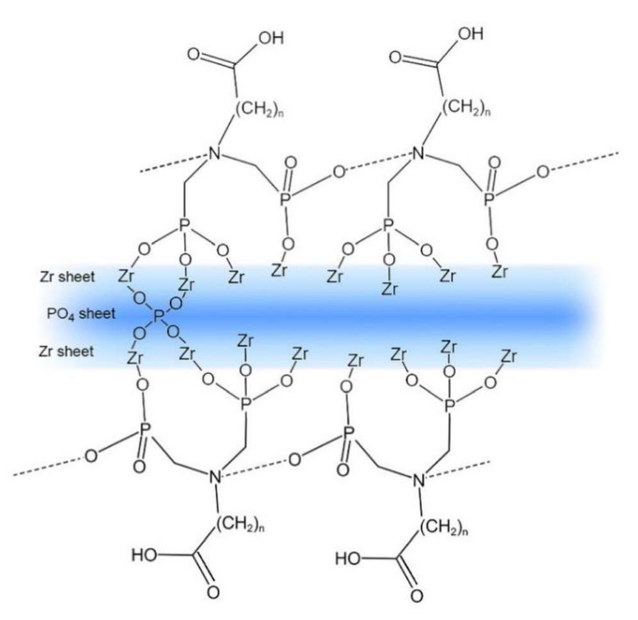

Fig. 1 Schematic structure of anhydrous ZGLY.

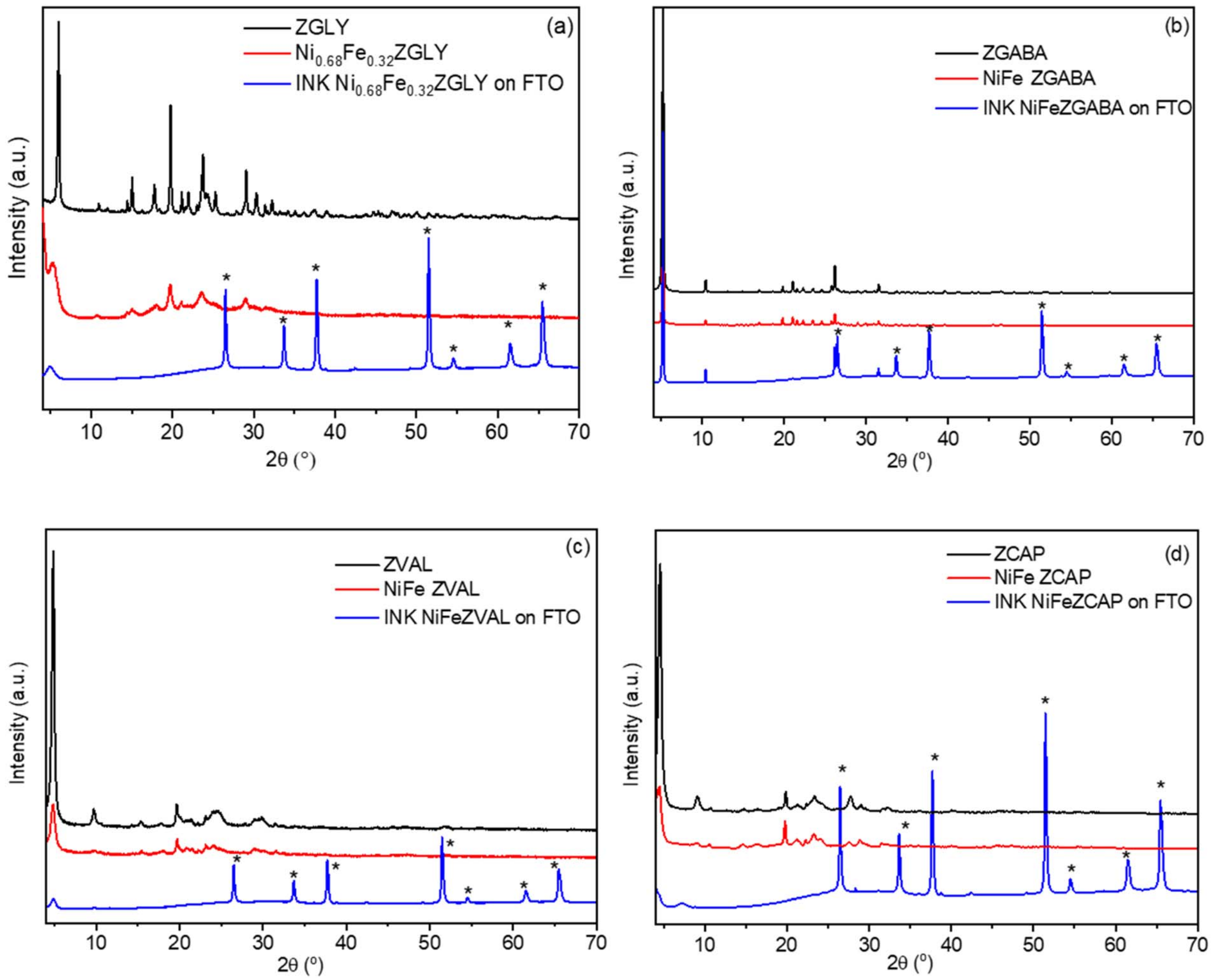

Fig. 2 XRD patterns of NiFeZPACs and the corresponding inks deposited on FTO compared with pristine ZGLY (ICSD No. 114801) (a), ZGABA (ICSD No. 115588) (b), ZVAL (ICSD No. 115589) (c), and ZCAP (d). * indicates the reflections of FTO.

structure due to the incoming of water inside the highly polar interlayer region, leading to the complete delamination of the material[23] and the formation of a stable colloidal dispersion of single lamellae or packets of a few lamellae. NiFeZPAC with varying metal compositions was prepared by mixing an aqueous colloidal dispersion of ZPAC with a solution of the metal salts with known molar fractions. The resulting dispersion was directly used to prepare the catalytic inks to be deposited on the glassy carbon electrode. The characterization of the materials was performed on the dried powders recovered from the colloidal dispersions. In terms of composition, it was observed that the Ni/(Fe + Ni) molar fraction in the solid is generally higher than the corresponding one in the feeding solution (see Table 1 columns 4 and 5), suggesting a high selectivity of the materials towards the divalent metal.[30] In addition, elemental analysis of the solids revealed the absence of propylamine, suggesting an ion-exchange reaction between propylammonium ions, formed during the treatment with propylamine, and the metal ions.

NiFeZPAC powders were also analyzed by XRD and ATR and compared with the plain ZPACs and with the corresponding ink deposited on FTO glass. The XRD patterns of the $Ni_{0.68}Fe_{0.32}$-ZGLY sample (Fig. 2a) exhibited a shift of the first reflection towards lower 2 theta angles (4.96°) with respect to ZGLY (5.97°) due to the intercalation of metal ions in the interlayer region. In addition, the low intensity and the increased broadening of the first reflection indicate a loss of order along the layer stacking direction (crystallographic *a*-axis). NiFeZGLY samples with different Ni molar fractions ($x_{Ni} = 0.89$; 0.48; 0.40) showed the same modification of the X-ray pattern (Fig. S1). Thus, only a partial restacking of the layers of the exfoliated material was achieved in NiFeZGLY, leaving a degree of disorder and potentially a high exposed area. As far as ZGABA, ZVAL and ZCAP are concerned, the immobilization of Ni^{2+} and Fe^{3+} did not induce an increase in the interlayer distance (Fig. 2b–d), probably due to the flexibility of the interlayer alkyl chains that can accommodate the metal ions in the free interlayer space available in these structures. The reflection intensities of NiFeZGABA are almost unchanged with respect to the original material, suggesting a reordering of the layers after the exchange of propylammonium with metal ions (Fig. 2b). A decrease in the intensity and an increase in the broadening of the first

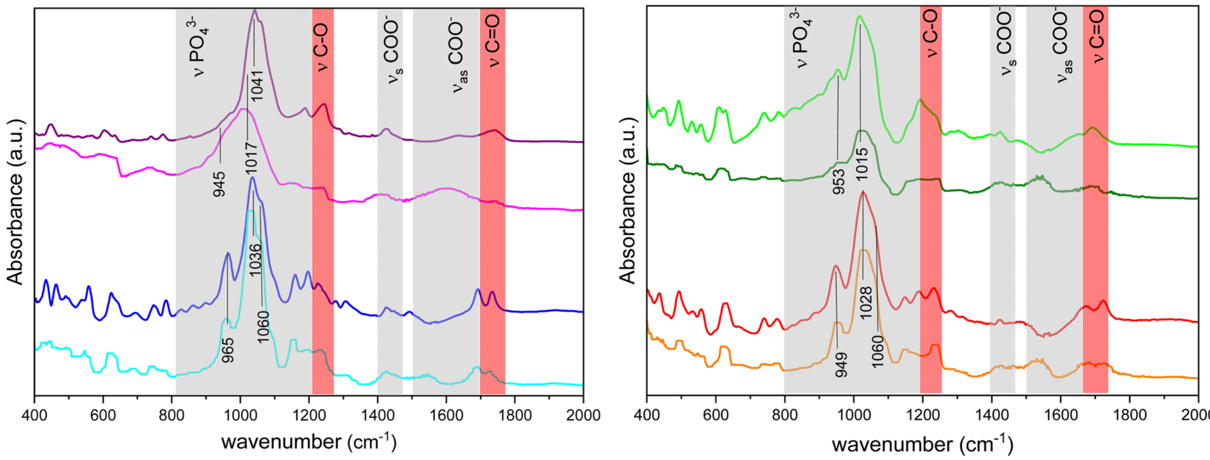

Fig. 3 ATR spectra of ZGLY (purple line) and $Ni_{0.68}Fe_{0.32}$ZGLY (magenta line); ZGABA (blue line) and NiFeZGABA (cyan line); ZVAL (green line) and NiFeZVAL (dark green line); ZCAP (red line) and NiFeZCAP (orange line) in the spectral region of 400–2000 cm^{-1}.

reflection of NiFeZVAL and NiFeZCAP are observed, indicating a certain degree of disorder, although less pronounced than that of NiFeZGLY (Fig. 2c and d). The XRD patterns of all the inks show reflections at low angles ascribable to the catalyst, confirming that its structure is retained in the ink.

Fig. 3 reports the ATR spectra of the NiFeZPACs in the 400–2000 cm^{-1} region, alongside those of the starting materials for comparison. The bands in the range 1700–1750 cm^{-1} of the pristine materials can be assigned to the asymmetric stretching of non-coordinated C═O and to the stretching of the COOH groups involved in hydrogen bonds, as reported previously.[22] After the immobilization of metal cations in NiFeZPACs, the signals of COOH groups are totally or partially replaced by the asymmetric and symmetric stretching vibrations of COO^- groups at 1650–

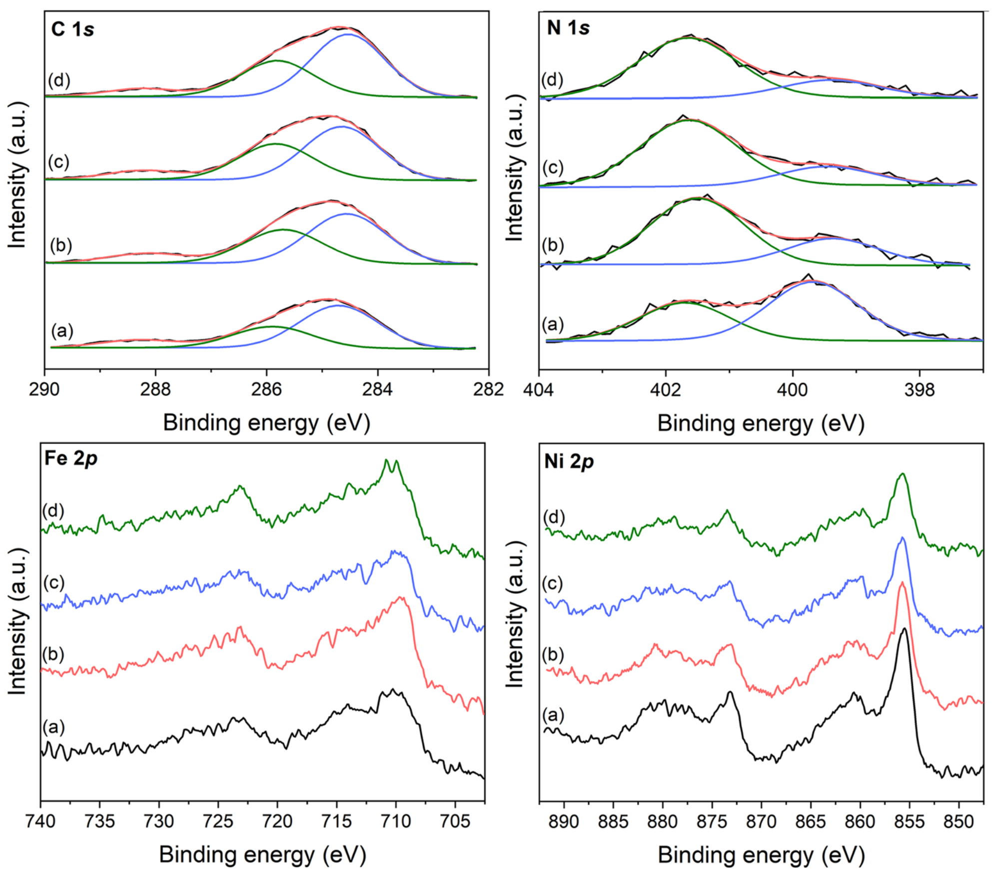

Fig. 4 High resolution C 1s, N 1s, Fe 2p and Ni 2p core level spectra of $Ni_{0.68}Fe_{0.32}$ZGLY (a), NiFeZGABA (b), NiFeZVAL (c) and NiFeZCAP (d).

1550 cm^{-1} and 1420 cm^{-1}, suggesting the interaction of metal cations with the pendant carboxylic groups. In the ZPAC spectra, the band at about 960 cm^{-1} is assigned to the ν_1 symmetric stretching vibration of PO_4^{3-}, the intense bands in the range 1020–1150 cm^{-1} are attributed to the ν_3 antisymmetric stretching vibrations of PO_4^{3-}, and the band at 1200 cm^{-1} is due to the P=O stretching. These bands remain unchanged in NiFeZGABA, NiFeZVAL and NiFeZCAP, while they are shifted towards lower wavenumbers in NiFeZGLY. This shift is indicative of different interactions of the phosphonic groups resulting from the exfoliation of the solid[22] and supports the XRD-based hypothesis that NiFeZGLY retains the high degree of disorder typical of colloidal dispersion. ATR spectroscopy shows a broader and weaker P–O peak compared to ZPACs, confirming a structural change and the presence of multiple P–O environments.

The surface of the catalysts in powder was studied by XPS. The survey spectra, not shown here, display the presence of all the expected constituent elements. Tables S1 and S2 list the surface chemical composition in atomic concentration% and the P/Zr, Zr/N and C/N atomic ratios (nominal and found), respectively. As expected, the carbon content increases with the increase of the length of the alkyl chain and concomitantly, the nitrogen content decreases. The P/Zr atomic ratios are always slightly higher than the nominal values (2.5). This is explained by the fact that P is more external than Zr and XPS is a very surface sensitive technique. Similarly, the Zr/N atomic ratios are always lower than the nominal values. Interestingly, the C/N found ratios are more or less similar to the nominal values. Therefore, XPS compositional analysis confirms the proposed composition. The high resolution C 1s core level spectra of the studied catalysts (Fig. 4) can be decomposed into three contributions at 284.5–284.7 eV, 285.7–285.9 eV, and 288.1–288.3 eV. The first contribution is assigned to adventitious carbon and –C–C– bonds, the second to C–N, C–P, and C–COO bonds, and the third to carboxylic groups. The high resolution N 1s spectra (Fig. 4) show two contributions at 399.4–399.7 eV and 401.7 eV. The former is assigned to R_3–N and the latter to R_3–NH^+. For the NiFeZCAP, NiFeZVAL, and NiFeZGABA samples, the spectra are dominated by the major peak corresponding to R_3–NH^+ species. Conversely, in $Ni_{0.68}Fe_{0.32}$ZGLY, the peak corresponding to R_3–N shows a prominent increase in intensity. This suggests enhanced metal-nitrogen coordination, facilitated by the short alkyl chain of the GLY moieties, which permits the simultaneous coordination of metal ions through both the carboxylic and nitrogen groups despite their lower basicity.[31] Interestingly, a clear trend is observed with the progressive elongation of the alkyl chain (from GLY to CAP): the relative contribution of the coordinated or free R_3–N species systematically decreases, while the protonated R_3–NH^+ signal becomes dominant. The high-resolution Fe 2p and Ni 2p core-level spectra are shown in Fig. 4, and their respective binding energy (BE) values are summarized in Table S3. These spectra display highly similar profiles and present a common trend: the Fe $2p_{3/2}$ and Ni $2p_{3/2}$ peaks appear at 710.1–709.5 eV and 855.4–855.7 eV, respectively, confirming the presence of Fe(III) and Ni(II). However, the BE values for Fe are shifted toward lower energies compared to $FeCl_3$ (711.3 eV) and lie close to those reported for Fe_2O_3 and/or FeOOH (710.60–710.95 eV and 710.20–710.60 eV), suggesting an oxygen-rich coordination environment around Fe^{3+} *via* the COO^- groups of the frameworks.[32] Regarding nickel, its BE values are higher than that of NiO (854.3 eV) and closely resemble those of Ni species interacting with carboxylate and amino groups, such as in Ni(2-aminobenzoate)$_2$ (855.9 eV),[31] which aligns with the observations made for the N 1s region. The high-resolution O 1s core-level spectra exhibit a main signal at 531.2–531.6 eV, which is attributed to carboxylate groups overlapping with the lattice oxygen of the phosphate/phosphonate matrix. In some cases, a weak contribution at 532.8–532.9 eV is detected, originating from P–OH groups. Notably, lattice oxygen associated directly with Fe or Ni was not observed. The high-resolution P 2p core-level spectra display a single symmetric signal at 133.1–133.4 eV, typical of P(V) species in phosphate/phosphonate environments. Finally, the high-resolution Zr 3d core-level spectra present a well-resolved Zr $3d_{5/2}$–Zr $3d_{3/2}$ doublet, with the Zr $3d_{5/2}$ peak located at 183.1–183.3 eV, which is characteristic of zirconium phosphate/phosphonate frameworks.

In order to investigate the distribution of the active metals on ZPACs, FE-SEM and EDS analyses were performed (Fig. S2). Elemental mapping of Zr, Ni, and Fe shows that these elements are uniformly distributed throughout the whole materials, confirming the immobilization of metal species on the particles.

To gain deeper insights at the nanoscale, the structural features of the NiFeZPAC samples were further investigated by STEM (Fig. 5). The STEM-BF images confirm the formation of thin, exfoliated nanosheets without the presence of crystalline metal nanoparticles or segregated phases.

EDS reveals a homogeneous spatial distribution of Ni and Fe species across the nanosheets, with no evidence of metal aggregation at the nanoscale. The uniform dispersion of metal ions within the hybrid framework supports the effectiveness of the amino acid-derived zirconium phosphate phosphonate structure in confining and stabilizing the precursors of the active species.

All catalyst inks were characterized by SEM before electrochemical testing (Fig. S3–S6). The images show that the as-deposited films consist of platelets horizontally oriented and partially fuse together, forming a nearly continuous film on the electrode surface. The morphology is not substantially altered by the addition of CNTs, and the catalysts appear well dispersed in the ink.

3.2 Electrochemical measurements

Several studies have established the overpotential at a current density of 10 mA cm^{-2}, referenced to the geometric surface area of the electrode, as a standard metric for evaluating OER performance. Accordingly, the electrocatalytic activity of ZPACs was assessed by comparing their overpotential at 10 mA cm^{-2}. The electrocatalytic performance of the NiFeZPAC materials toward the oxygen evolution reaction was evaluated in alkaline media using cyclic voltammetry (CV) and linear sweep voltammetry (LSV). For consistency, the overpotential (η_{10}) required to reach a geometric current density of 10 mA cm^{-2} was adopted as

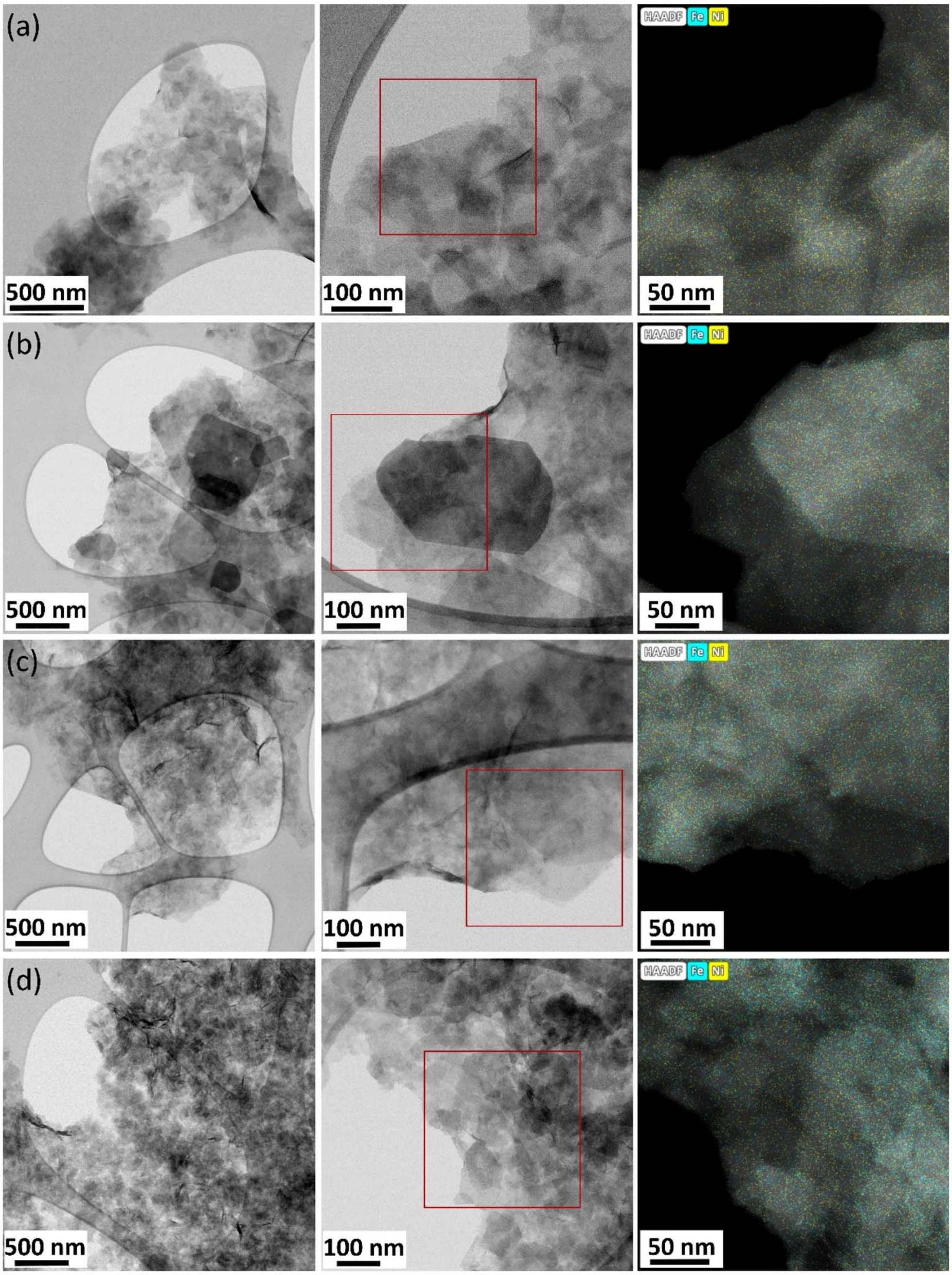

Fig. 5 STEM-BF images at different magnifications and EDS elemental mapping of $Ni_{0.68}Fe_{0.32}$ZGLY (a), NiFeZGABA (b), NiFeZVAL (c) and NiFeZCAP (d). EDS of Ni (yellow) and Fe (cyan) species within the hybrid framework.

the primary benchmarking parameter. The η_{10} values for each catalytic system were obtained by averaging the measurements from the first CV of three independently prepared working electrodes. The metal-free ZPACs exhibit negligible OER activity within the investigated potential window, confirming that the zirconium phosphate–phosphonate framework acts as an electrochemically inert but structurally and chemically robust support. Notably, the incorporation of iron has been demonstrated to be essential for these high-efficiency catalysts. However, the best doping concentration of Fe is indicated as quite controversial in the literature.[33–35] Therefore, initial studies were carried out on the system ZGLY in order to optimize the Ni/Fe ratio in terms of electrocatalytic performance. Fig. 6 displays the cyclic voltammograms for the composites with varying Fe content. As expected, Ni-functionalized ZGLY shows measurable OER activity, although with a relatively high overpotential of 596 mV (Fig. 6) to achieve a geometric current density of 10 mA cm^{-2}.

The incorporation of Fe markedly enhances the catalytic performance, in line with the well-established synergistic effect

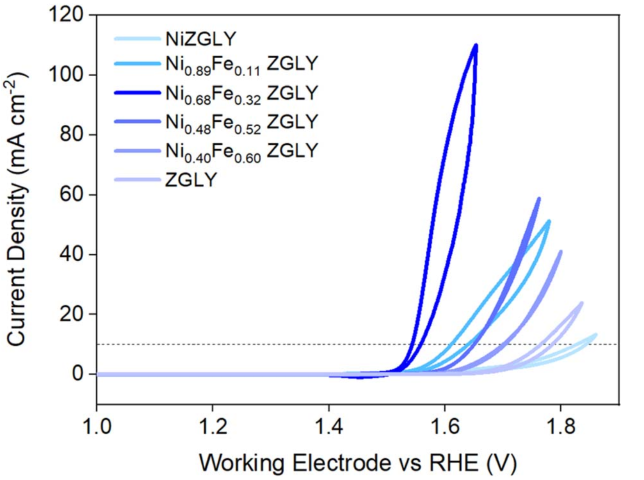

Fig. 6 Cyclic voltammetry curves for all synthesized NiFeZGLY in 0.1 M KOH with a scan rate of 100 mV s^{-1}. The CV curve of ZGLY was reported for comparison.

between Ni and Fe in alkaline OER catalysis.[35] Systematic variation of the Ni/Fe ratio in the ZGLY-based materials reveals a clear composition-dependent trend, with the lowest overpotential (304 mV) obtained for a $Ni_{0.68}Fe_{0.32}$ZGLY composition. Further increases in Fe content led to higher overpotentials, as seen for $Ni_{0.48}Fe_{0.52}$ZGLY (420 mV) and $Ni_{0.40}Fe_{0.60}$ZGLY (470 mV), indicating a decline in activity beyond the optimal composition (Fig. 7A). These results highlight a synergistic effect between Ni and Fe within the zirconium phosphonate framework, where balanced metal incorporation enhances charge transfer and active site efficiency, while excessive Fe content diminishes the catalytic performance. The observed optimal composition is consistent with literature reports on Ni–Fe (oxy)hydroxide systems,[35] while emphasizing the role of the zirconium phosphonate framework in stabilizing an efficient interfacial arrangement of the two metals. Further insight into the reaction kinetics is provided by Tafel analysis derived from LSV measurements (Fig. 7B). The Tafel slope decreases significantly upon Fe incorporation, reaching a minimum value of approximately 32.9 mV dec^{-1} for $Ni_{0.68}Fe_{0.32}$ZGLY. This low slope is indicative of fast reaction kinetics and suggests that the rate-determining step is effectively facilitated by the cooperative interaction between Ni and Fe centers confined at the interface. At higher Fe contents, the increase in the Tafel slope reflects the decline in catalytic activity, reinforcing the existence of an optimal metal ratio for efficient catalysis.

Based on these findings, catalysts incorporating longer carbon chains were synthesized using an iron concentration corresponding to the optimized value identified for the ZGLY system.

The cyclic voltammograms of the resulting NiFeZPACs are shown in Fig. 8, with the corresponding overpotentials at 10 mA cm^{-2} summarized in Table 2.

A comparison among NiFeZPACs derived from different amino acid ligands reveals that all systems exhibit relatively similar overpotentials (304–332 mV). The OER activities of these different ZPACs confirmed the powerful synergy between the Ni and Fe active sites present on the catalyst surface.

The cyclic voltammograms also display characteristic precatalytic redox features associated with the Ni^{2+}/Ni^{3+} transformation, commonly attributed to the $Ni(OH)_2$/NiOOH redox couple in alkaline electrolytes. For NiFeZGABA, NiFeZVAL and NiFeZCAP, this redox process is clearly observed, whereas it is less distinct for NiFeZGLY. This behavior can be attributed to the higher OER current density in NiFeZGLY, which hides the redox signal and suggests an earlier onset of catalytically active NiOOH species. As previously reported, increasing Fe content in Ni–Fe systems is commonly associated with a shift of the Ni^{2+}/Ni^{3+} redox couple toward higher potentials. At sufficiently high Fe concentrations, the redox feature becomes indistinguishable, coinciding with the sharp onset of the OER current and thereby no longer detectable in the voltammograms. This observation supports the idea that Fe modifies the electronic

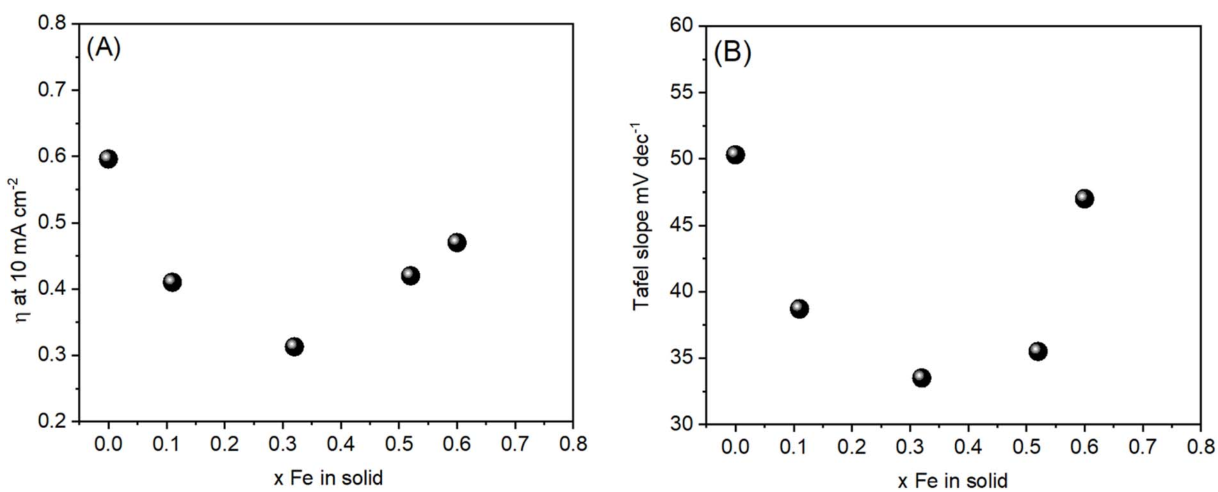

Fig. 7 Overpotential of NiFeZGLY required for a current density of 10 mA cm^{-2} in 0.1 M KOH (A) and Tafel slope (B) as a function of the Fe molar fraction (x) in the catalyst.

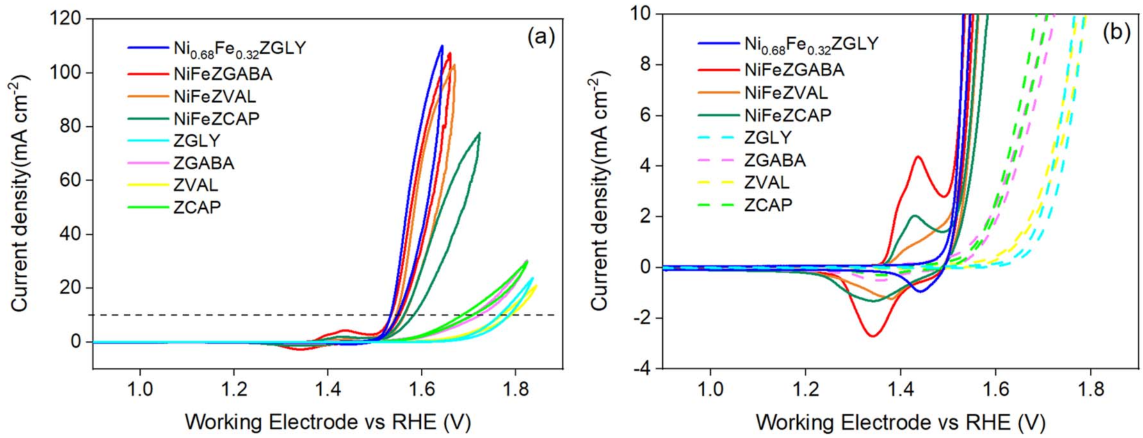

Fig. 8 Cyclic voltammetry curves for all synthesized NiFeZPACs in 0.1 M KOH with a scan rate of 100 mV s^{-1}. Cyclic voltammetry curves for ZPACs were added for comparison (a). Enlargement of the CV curves in the current density range from −4 to 10 mA cm^{-2} (b).

Table 2 Experimental overpotentials of NiFeZPACs obtained at $j = 10$ mA cm^{-2}

Sample	η_{10} (mV)
$Ni_{0.68}Fe_{0.32}$ZGLY	304
NiFeZGABA	305
NiFeZVAL	315
NiFeZCAP	332

structure of Ni centers and promotes the formation of highly active NiOOH-type species during electrochemical operation.[35]

Tafel plots for each system were derived from LSV measurements (Fig. 9a), and representative curves are shown in Fig. 9b.

The Tafel slopes of the NiFeZPAC catalysts fall within a narrow range of 32.9 to 52 mV dec^{-1} (Table 3), indicating comparable intrinsic catalytic kinetics. These values are comparable to those reported for $Ni_{1-x}Fe_xOOH$ thin films,[28] suggesting a similar mechanism for the OER in all systems.

To place the performance of the NiFeZPAC catalysts in a broader context, their OER activity was benchmarked against representative state-of-the-art Ni–Fe based electrocatalysts reported in the literature (Table S4). As shown, the optimized $Ni_{0.68}Fe_{0.32}$ZGLY catalyst exhibits an overpotential of approximately 304 mV at a geometric current density of 10 mA cm^{-2}, which is slightly higher than that of widely studied hybrid systems operating in alkaline media. The corresponding Tafel slope of 32.9 mV dec^{-1} falls within the lower range reported for highly active Ni–Fe based catalysts, indicating favorable reaction kinetics.

To comprehensively evaluate the electrocatalytic performance of the NiFeZPACs, several key parameters were analyzed, including ECSA, roughness factor (RF) and TOF. ECSA was estimated from the double-layer capacitance (C_{dl}) measured *via* CV in the non-faradaic region (Fig. S7–S10) and normalized by a standard specific capacitance of 40 μF cm^{-2}.[28] The ECSA values of the NiFeZPAC catalysts are comparable across the

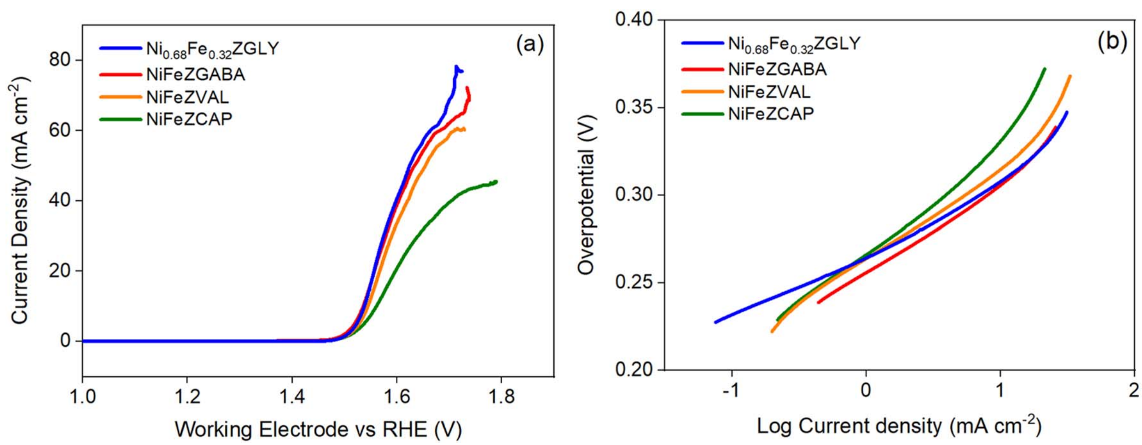

Fig. 9 Linear sweep voltammograms (a) and Tafel plots (b) for NiFeZPAC-based catalysts.

Table 3 Tafel slope values of NiFeZPACs

Sample	Tafel slope (mV dec^{-1})
$Ni_{0.68}Fe_{0.32}$ZGLY	32.9
NiFeZGABA	45.8
NiFeZVAL	48.0
NiFeZCAP	52.0

Table 4 ECSA, RF and TOF @ η = 350 mV for NiFeZPACs

Sample	ECSA (cm^2)	RF	TOF (s^{-1})
$Ni_{0.68}Fe_{0.32}$ZGLY	0.68	9.62	0.047
NiFeZGABA	0.56	8.21	0.035
NiFeZVAL	0.84	11.89	0.029
NiFeZCAP	0.66	9.34	0.017

series (Table 4), indicating that the observed differences in OER activity cannot be ascribed to variations in the electrochemically accessible surface area. Instead, the enhanced performance of selected compositions reflects differences in the nature,

Table 5 Ni loading in the ink, j @ η = 350 mV, and mass activity @ η = 350 mV

Sample	Ni (µg)	j_{350} (mA cm^{-2})	M. A.$_{350}$ (A g^{-1})
$Ni_{0.68}Fe_{0.32}$ZGLY	7.49	32.4	4328
NiFeZGABA	9.52	30.6	3215
NiFeZVAL	9.58	26.1	2725
NiFeZCAP	9.68	15.4	1591

accessibility, and local coordination environment of the interfacial Ni–Fe active sites. These results highlight that chemical confinement within the zirconium phosphate phosphonate framework governs the effectiveness of Ni–Fe interactions and plays a key role in dictating OER activity.

Based on a geometric electrode area of 0.0707 cm^2, the RF values of the NiFeZPAC catalysts were calculated to range from 8.21 to 11.89 (Table 4). These relatively low roughness factors are consistent with the planar morphology of the ZPAC structures. As observed in the SEM images (Fig. S3–S6), the exfoliated nanosheets tend to align predominantly parallel to the

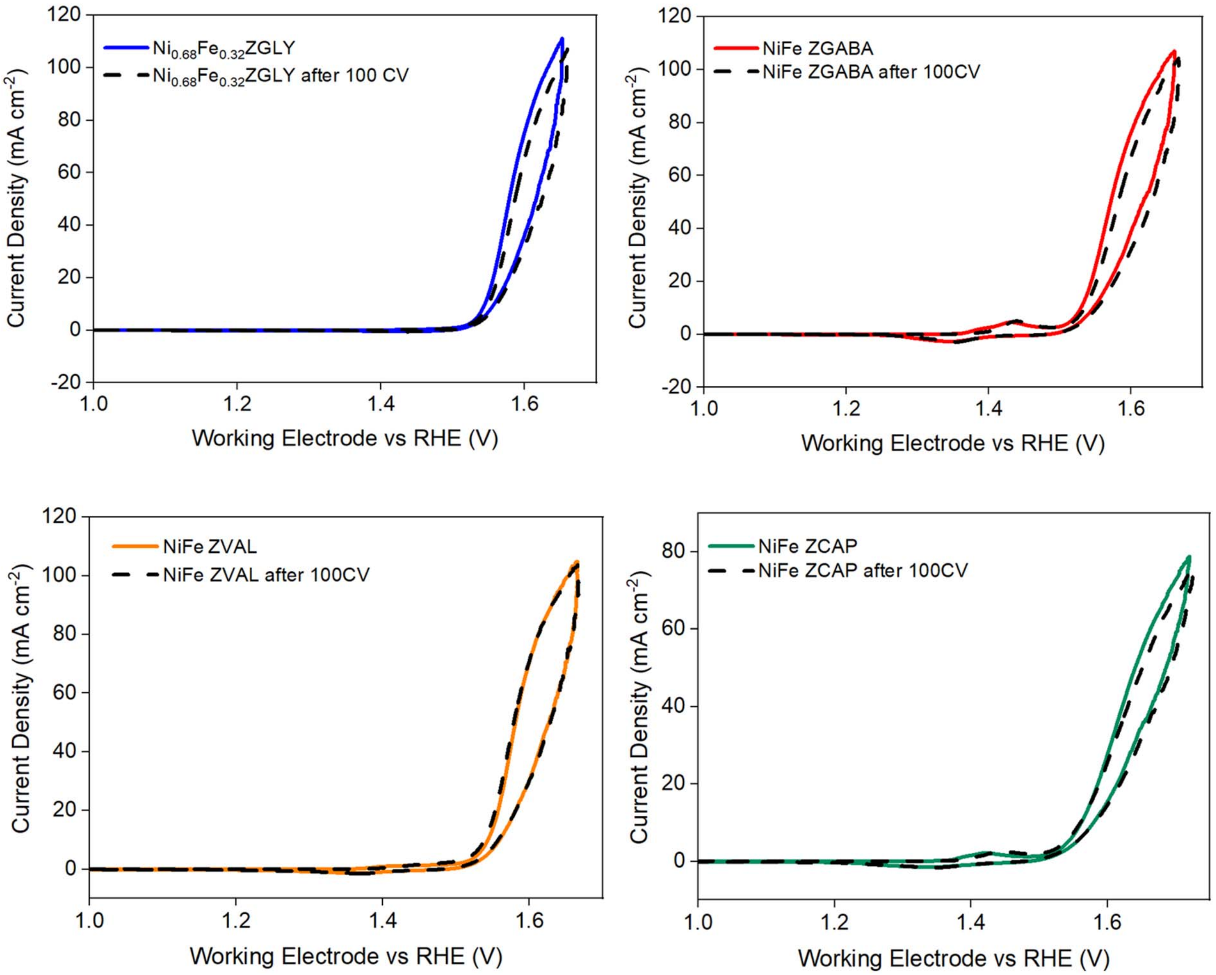

Fig. 10 Comparison of the 1st (colored line) and 100th (black dashed line) cyclic voltammograms of NiFeZPACs recorded in 0.1 M KOH at a scan rate of 100 mV s^{-1}.

substrate during ink deposition, which limits surface corrugation and results in modest roughness values.

The TOF of the ZPAC catalysts ranges from 0.047 to 0.017 s^{-1} at an overpotential of 350 mV, with the highest and lowest values observed for NiFeZGLY and NiFeZCAP, respectively, assuming that all metal atoms drop-cast onto the glassy carbon electrode participate in the OER. As commonly encountered for heterogeneous Ni–Fe-based OER catalysts, this assumption likely leads to an underestimation of the intrinsic activity, since only a fraction of the metal centers is expected to be electrochemically accessible under operating conditions. Accordingly, the reported TOF values should be regarded as apparent, lower-bound estimates that are primarily meaningful for comparative analysis within the ZPAC series rather than as absolute intrinsic metrics. The TOF values obtained in this work fall within the range reported for representative Ni-based and Ni–Fe-based OER catalysts, as well as benchmark IrO_x systems (Table S5). It should be noted that literature TOF values are often derived using different assumptions regarding the number of active sites, and therefore the comparison is primarily qualitative.[36] Notably, the relatively narrow TOF range among NiFeZGLY, NiFeZGABA and NiFeZVAL is consistent with their comparable overpotential values (304–315 mV at 10 mA cm^{-2}) and with the EIS results, which reveal moderate but limited variations in the charge-transfer resistance (R_{ct}), with values ranging from 48 to 67 Ω (Fig. S11). In contrast, the lower TOF observed for the ZCAP-based catalyst correlates with its higher overpotential (332 mV), suggesting a reduced utilization of active Ni–Fe sites rather than a fundamentally different active-site chemistry.

In order to investigate the intrinsic performance of these catalytic systems, the mass-normalized activities at an OER overpotential of 350 mV were calculated for ZPAC catalysts, taking into account the Ni loading in the amount of catalyst used, determined from ICP-OES measurements. Mass activity provides a practical metric of catalyst efficiency by normalizing the OER current to the catalyst mass, thereby reflecting the effective utilization of active species within the material. The mass activity of the NiFeZPAC catalysts shows a clear decreasing trend from NiFeZGLY to NiFeZCAP, with values of 4328, 3215, 2726, and 1592 A g^{-1}, respectively, evaluated at the same overpotential (Table 5). This trend closely reflects the behavior observed for the apparent TOF and overpotential values, offering the additional advantage of a chemically tunable hybrid framework enabling controlled metal confinement. The higher mass activity of NiFeZGLY can be attributed to its higher degree of exfoliation and structural disorder, which enhances catalyst dispersion and accessibility of electrochemically active sites. In contrast, the significantly lower mass activity observed for NiFeZCAP is consistent with its higher overpotential and reduced TOF, suggesting limitations in active-site accessibility and interfacial exposure. Overall, the results highlight that catalytic performance is not solely governed by surface area or morphology, but is strongly influenced by the chemical environment and confinement of the active species within the hybrid framework.

To assess the stability of the catalyst under operating conditions, the CV analysis was repeated on the material after 100 cycles. As shown in Fig. 10, the comparison between the first and the 100th cyclic voltammograms recorded in 0.1 M KOH reveals only minor changes in the overall voltammetric response for the NiFeZPAC catalysts. In particular, the samples exhibit a largely preserved current profile after repeated cycling, indicating good electrochemical robustness of the interfacial Ni–Fe sites under alkaline conditions.

In order to study the structural stability of the catalysts after electrochemical measurements by XRD analysis, the inks were deposited on an FTO electrode and the electrochemical tests were repeated (Fig. 11). Notably, the catalytic performance was not affected by the support used. After electrochemical treatment in 0.1 M KOH for 100 cycles, no structural changes were observed. The patterns are primarily characterized by diffraction peaks arising from the FTO substrate, while only weak reflections attributable to the catalyst are detected at low 2θ values, consistent with the presence of the layered solids. The low intensity of the catalyst reflections suggests a low loading and/or high degree of exfoliation of the active phase on the FTO surface, with no evidence of additional crystalline impurities. Additionally, EDS elemental mapping confirms a uniform distribution of Ni and Fe within the ZPAC layers, after treatment with 0.1 M KOH solution and following 100 cycles of cyclic voltammetry (Fig. S3–S6).

Raman and XPS spectroscopy were employed to investigate the structural evolution of the NiFeZPAC inks deposited on an FTO electrode, induced by the electrochemical treatment. Fig. 12 compares the Raman spectra collected before and after the reaction. The overlaid spectra clearly highlight the formation of new active phases following electrochemical conditioning. The most pronounced modifications occur in the 400–700 cm^{-1} region, where the appearance of a band at ≈460 cm^{-1} and the progressive definition of features in the 520–650 cm^{-1} range are observed after the reaction. These bands are

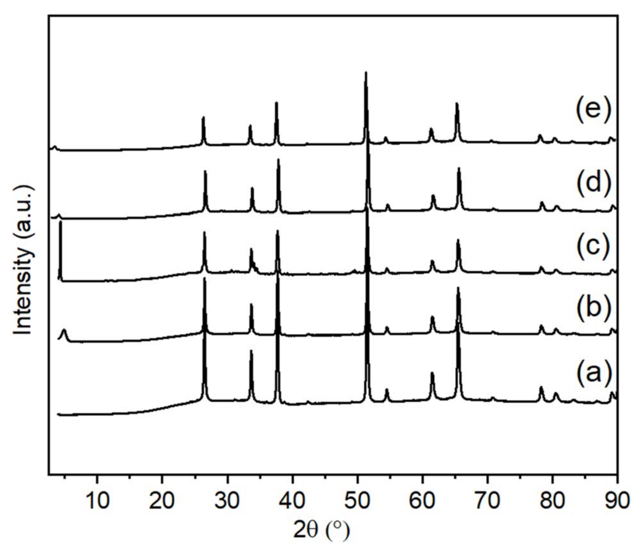

Fig. 11 XRD patterns of NiFeZPACs on FTO after 100 CV cycles. (a) FTO, (b) $Ni_{0.68}Fe_{0.32}$ZGLY, (c) NiFeZGABA, (d) NiFeZVAL and (e) NiFeZCAP.

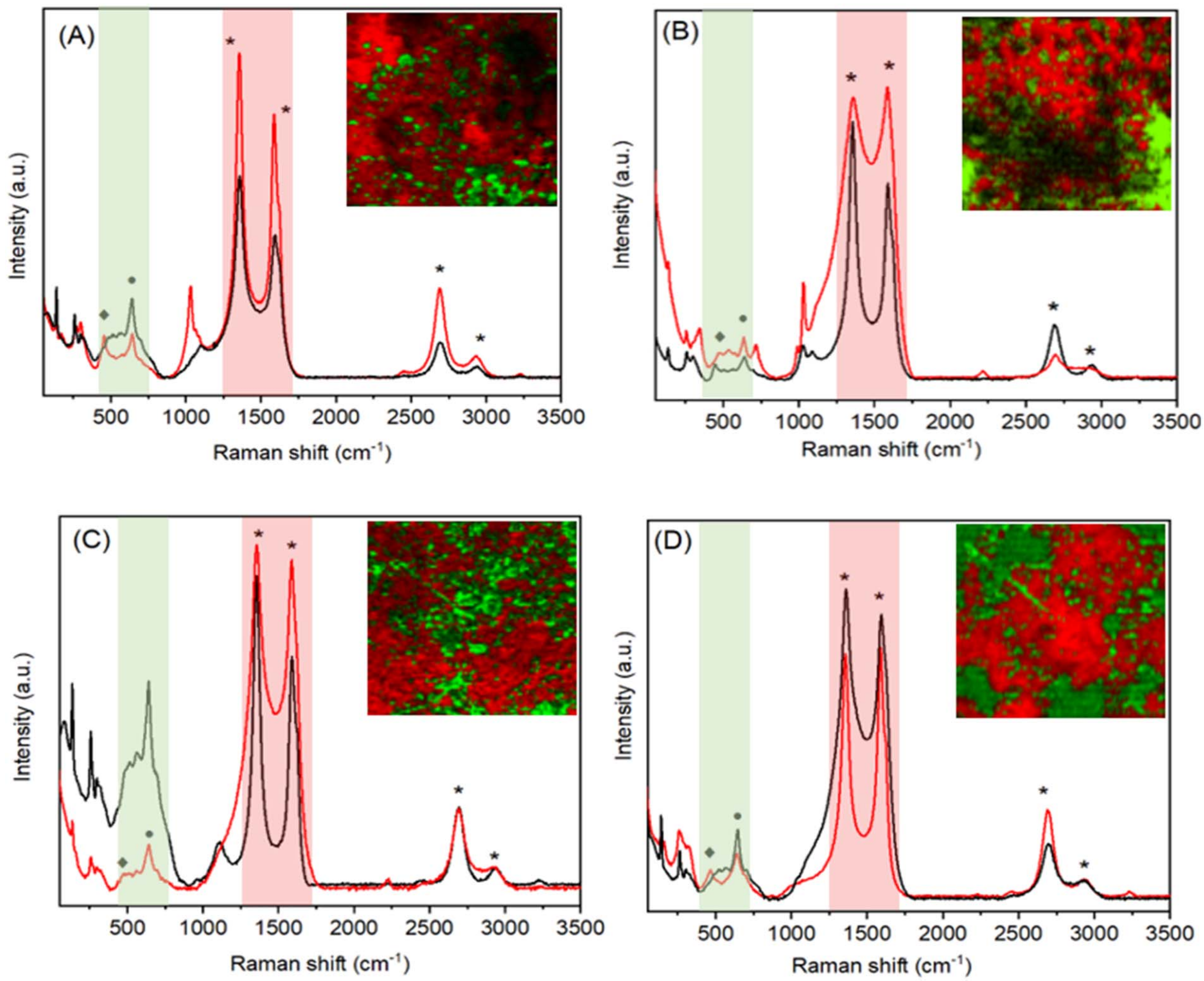

Fig. 12 Raman spectra recorded before (black line) and after (red line) the electrochemical reaction for (A) $Ni_{0.68}Fe_{0.32}$ZGLY, (B) NiFeZGABA, (C) NiFeZVAL, and (D) NiFeZCAP inks. Asterisks (*) indicate bands attributable to CNTs; diamonds (◆) denote NiOOH-type vibrational modes; circles (●) mark Fe oxide/oxyhydroxide vibrations. Insets show representative Raman 2D maps collected after the reaction. Combined color maps are reported for NiFeZPACs, where CNTs are shown in red and NiOOH/Fe oxide–oxyhydroxide species formed after the reaction are shown in green.

attributable to NiOOH-type vibrations (notably the characteristic $\approx$460 cm^{-1} mode) and Fe oxide/oxyhydroxide species, indicating partial oxidation of Ni^{2+} to NiOOH and the concurrent formation of Fe-based oxyhydroxides during electrochemical operation, in agreement with previous reports on Ni–Fe electrocatalysts. The relative intensity of the NiOOH- and Fe-related bands differs among NiFeZGLY, NiFeZGABA, NiFeZVAL and NiFeZCAP, suggesting that the ligand environment modulates the extent of surface reconstruction of the electrochemically generated active phase. The insets in Fig. 12 display representative post-reaction 2D Raman maps. The combined colour maps (red = CNTs; green = NiOOH/Fe oxide-oxyhydroxide species) reveal a heterogeneous but well-dispersed distribution of the oxidized Ni–Fe domains across the carbon network. Although all samples undergo surface activation consistent with electrocatalytic oxidation, clear differences in the spatial distribution and relative abundance of NiOOH and Fe oxide/oxyhydroxide species are observed, reflecting variations in the composition and structure arising from the different ligands. These results support a correlation between the redox behaviour, the spectroscopic signature of the NiOOH-type phase in the ZPAC electrocatalysts, and their OER activity.[35]

The interpretation of the XPS spectra is somewhat complicated by the high fluorine content originating from the Nafion binder. Specifically, the F_{KLL} Auger signal (859.0 eV) overlaps with the high-resolution Ni 2p core level spectra (Fig. 13). This spectral overlap is more pronounced for the inks formulated with NiFeZGABA and $Ni_{0.68}Fe_{0.32}$ZGLY, which exhibit higher fluorine concentrations (Table S6). Nonetheless, the Ni $2p_{3/2}$ peak displays a new contribution or a shift toward higher binding energies compared to the pristine catalysts (Fig. 13). These binding energy values are centered at 856.1–856.2 eV for NiFeZGABA, NiFeZVAL, and NiFeZCAP. Conversely, for the NiFeZGLY ink, only a high-energy shoulder is discerned. The appearance of this peak component at 856.2 eV is indicative of

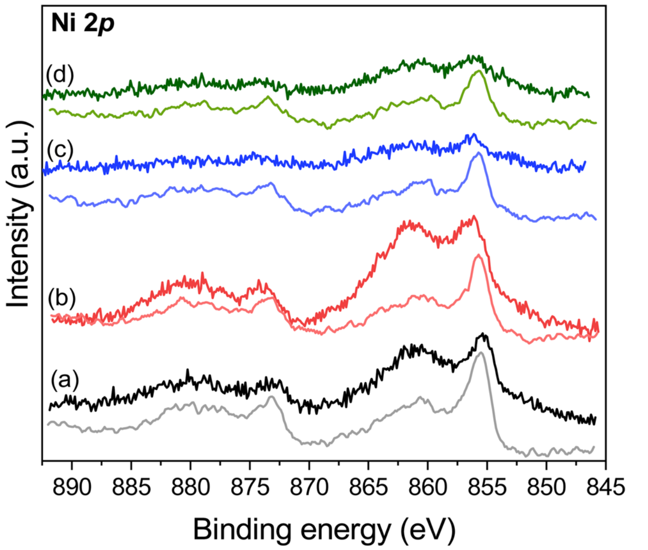

Fig. 13 High resolution Ni 2p core level spectra of $Ni_{0.68}Fe_{0.32}$ZGLY (a), NiFeZGABA (b), NiFeZVAL (c) and NiFeZCAP (d), before (light color) and after (dark color) the electrochemical tests.

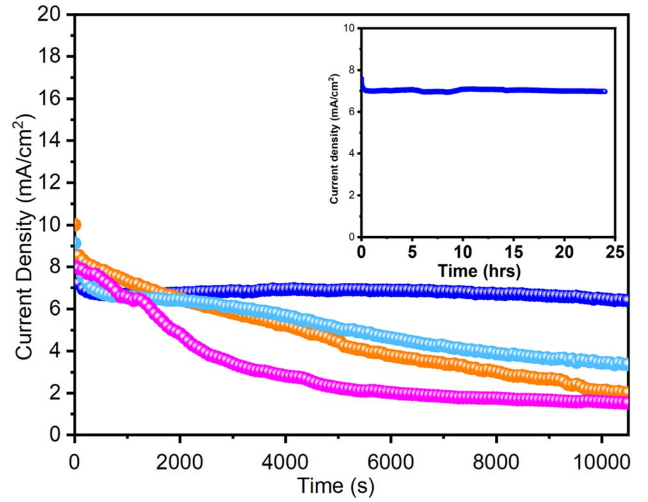

Fig. 14 Chronoamperometric data of $Ni_{68}Fe_{0.32}$ZGLY (blue line), NiFeZGABA (orange line), NiFeZVAL (light blue line), and NiFeZCAP (pink line). The inset shows the long-term chronoamperometric stability test of $Ni_{0.68}Fe_{0.32}$ZGLY over 24 h.

the formation of NiOOH species[37] in agreement with the complementary Raman spectroscopy findings. The high-resolution Fe 2p core-level spectra exhibit a relatively low signal-to-noise ratio due to the low iron content within the samples, making the precise identification of the Fe $2p_{3/2}$ peak position challenging. Nevertheless, for the ink based on NiFeZVAL and NiFeZCAP, distinct peak maxima are observed at 710.5 eV and 710.6 eV, respectively, which can be confidently ascribed to FeOOH species.[32] The structural transformations, observed *via* Raman and XPS spectroscopy, suggest an electrochemically driven surface reconstruction that promotes the *in situ* growth of active FeOOH/NiOOH phases, directly contributing to enhanced electrocatalytic performance.

Operational stability is an important parameter for evaluating the practical applicability of electrocatalysts toward the oxygen evolution reaction. The electrochemical robustness of the NiFeZPAC catalysts was therefore further evaluated by chronoamperometric measurements in 0.1 M KOH, in which each catalyst was held at the potential required to sustain a current density of 10 mA cm^{-2} while monitoring the current response over time. As shown in Fig. 14, the $Ni_{0.68}Fe_{0.32}$ZGLY catalyst maintains a nearly constant current density during the measurement, indicating superior operational stability compared to the other members of the series. In contrast, zirconium phosphonates bearing longer alkyl chains exhibit a gradual decrease in current, suggesting a less stable interfacial configuration under alkaline OER conditions. The present results highlight the critical role of the ligand structure and interfacial accessibility in determining both catalytic activity and operational stability within the ZPAC series.

Building on these observations, the long-term stability of the most promising sample, $Ni_{0.68}Fe_{0.32}$ZGLY, was further evaluated by chronoamperometry over 24 h under continuous OER operation (Fig. 14, inset). An initial decrease in current density is observed within the first minutes, which can be attributed to surface restructuring and activation processes commonly reported for Ni–Fe-based catalysts. After this initial stage, the current density stabilizes and remains nearly constant over the entire duration of the test, with negligible loss of activity, confirming the excellent electrochemical durability of the catalyst under alkaline conditions. The sustained performance suggests that the zirconium phosphate–phosphonate framework effectively stabilizes the catalytically active species and prevents their aggregation or deactivation during prolonged operation. While the present results demonstrate good durability under laboratory conditions, extended testing under practically relevant conditions remains an important objective for future studies. To further assess the structural and chemical integrity of $Ni_{0.68}Fe_{0.32}$ZGLY under prolonged operating conditions, post-*operando* characterization was performed after the 24 h chronoamperometric test. XRD patterns collected after extended operation are indistinguishable from those obtained after 100 CV cycles, with no new crystalline phases and full retention of the low-angle reflections characteristic of the layered ZPAC scaffold (Fig. S12). Raman spectra recorded after 24 h operation are fully consistent with those obtained after cycling, with the NiOOH band at ~460 cm^{-1} and the Fe-oxyhydroxide features in the 520–650 cm^{-1} region unchanged in position and relative intensity (Fig. S12), confirming that the active oxyhydroxide phase reaches a stable chemical state during the initial activation transient and does not evolve further under sustained OER conditions. SEM images confirm that the film retains its platelet-like morphology with no evidence of agglomeration or dissolution and EDS elemental mapping demonstrates a uniform spatial distribution of Ni, Fe, Zr, and P, ruling out metal leaching or phase segregation (Fig. S13). Taken together, these results demonstrate that the ZPAC framework acts as a chemically robust host that confines and stabilizes the catalytically active NiOOH/FeOOH species, preventing their aggregation and deactivation that commonly limit the long-term performance of unsupported Ni–Fe electrocatalysts.

4. Conclusion

This study demonstrates that amino acid-derived zirconium phosphate phosphonates constitute an effective and chemically versatile platform for the rational design of interface-confined Ni–Fe active sites for alkaline oxygen evolution reaction. Controlled exfoliation of the layered zirconium phosphonate framework enables homogeneous immobilization of Ni^{2+} and Fe^{3+} ions at organic–inorganic interfaces, allowing precise tuning of metal composition, coordination environment, and accessibility of catalytically active sites. Systematic variation of the Ni/Fe ratio reveals a clear composition–performance relationship, with the optimized $Ni_{0.68}Fe_{0.32}$ZGLY catalyst delivering competitive OER activity, characterized by an overpotential of approximately 304 mV at 10 mA cm^{-2} and a low Tafel slope of 32.9 mV dec^{-1}. While these values are comparable to those of state-of-the-art Ni–Fe-based electrocatalysts, the present system distinguishes itself through the use of a chemically robust zirconium phosphonate framework that provides well-defined interfacial confinement and enhanced structural stability under alkaline conditions. Among the investigated materials, the glycine-derived zirconium phosphonate exhibits superior mass activity and electrochemical robustness, which can be attributed to its higher degree of exfoliation and the persistence of structural disorder, maximizing interfacial exposure of Ni–Fe active species.

Post-*operando* Raman spectroscopy and XPS identify the *in situ* formation of NiOOH and FeOOH as the principal catalytically active phases, which are effectively stabilized by the zirconium phosphonate framework, mitigating aggregation and structural degradation under alkaline conditions. Crucially, the ZPAC framework suppresses the aggregation and deactivation of these transient phases, as confirmed by structural analyses after 100 CV cycles. Among the investigated samples, $Ni_{0.68}Fe_{0.32}$ZGLY exhibited the highest stability, maintaining its framework integrity and homogeneous metal distribution after prolonged chronoamperometric testing under OER operating conditions. Taken together, these results reframe the role of the ZPAC host: rather than a passive support, it functions as an active chemical environment that stabilizes transient oxyhydroxide phases, tunes their nucleation density and controls their long-term persistence under alkaline operation. This work establishes interfacial confinement within exfoliated, organically functionalized zirconium phosphonate layers as a general and transferable strategy for designing durable, earth-abundant OER electrocatalysts, with straightforward extension to other first-row transition metal combinations and to the broader class of multi-electron electrochemical energy conversion reactions.

Author contributions

A. D., M. N.: conceptualization, methodology, supervision, data curation, writing – original draft, and writing – review and editing. I. D.: investigation and data curation. G. M. R. and R. V.: data curation and writing – review and editing. S. G.: investigation and data curation. B. M.: investigation and data curation. E. R. C.: investigation, data curation, and writing – review and editing. A. M. and F. C.: writing – review and editing, project administration, and funding acquisition.

Conflicts of interest

The authors declare no competing financial interest.

Data availability

The authors confirm that the data supporting the findings of this study are available within the article and its supplementary information (SI). Supplementary information is available. See DOI: https://doi.org/10.1039/d6ta01464j.

Acknowledgements

This work has been funded by the European Union – NextGenerationEU under the Italian Ministry of University and Research (MUR) National Innovation Ecosystem grant ECS00000041 – VITALITY. We acknowledge the Università degli Studi di Perugia and MUR for support within the project Vitality and the Fondazione Perugia through Bando di Ricerca Scientifica 2023 (ID21101). A. D and A. M. also acknowledge funding from the Fondo Ricerca di Ateneo, edition 2021. G. M. R. and A. M. also acknowledge funding from the Presidency of the Council of Ministers of Italy – Department for Cohesion Policies and the South, under the UMbriaTECH – Umbria Materials TECHnology project (CUP E67G23000220001) and Progetto Competitivo 2024, CMPT248870. B. M. also thanks the Center for Electronic Microscopy (Ce.ME) – Laura Bonzi at the ICCOM-CNR in Florence. E. R. C. acknowledges financial support from project PID2021-126235OB-C32 funded by MCIN/AEI/10.13039/501100011033 and FEDER funds, and the financial support of UNICAJA and Erasmus+ for H2EXCELLENCE.

References

1 I. Dincer, *Int. J. Hydrogen Energy*, 2012, **37**, 1954–1971.
2 M. Awad, A. Said, M. H. Saad, A. Farouk, M. M. Mahmoud, M. S. Alshammari, M. L. Alghaythi, S. H. E. Abdel Aleem, A. Y. Abdelaziz and A. I. Omar, *Alexandria Eng. J.*, 2024, **87**, 213–239.
3 J. Song, C. Wei, Z.-F. Huang, C. Liu, L. Zeng, X. Wang and Z. J. Xu, *Chem. Soc. Rev.*, 2020, **49**, 2196–2214.
4 G. Menendez Rodriguez and A. Macchioni, *Eur. J. Inorg. Chem.*, 2023, **26**, e202200625.
5 L. Gao, X. Cui, C. D. Sewell, J. Li and Z. Lin, *Chem. Soc. Rev.*, 2021, **50**, 8428–8469.
6 L. Fagiolari, F. Zaccaria, F. Costantino, R. Vivani, C. K. Mavrokefalos, G. R. Patzke and A. Macchioni, *Dalton Trans.*, 2020, **49**, 2468–2476.
7 L. Baldinelli, G. Menendez Rodriguez, I. D'Ambrosio, A. M. Grigoras, R. Vivani, L. Latterini, A. Macchioni, F. De Angelis and G. Bistoni, *Chem. Sci.*, 2024, **15**, 1348–1363.

8 P. Roy Chowdhury, H. Medhi, K. G. Bhattacharyya and C. M. Hussain, *Coord. Chem. Rev.*, 2024, **501**, 215547.
9 L. Fagiolari and A. Macchioni, in Progress in Layered Double Hydroxides from Synthesis to New Applications, *Series on Chemistry, Energy and the Environment*, ed. K. M. Kadish and R. Guilard, World Scientific Publishing, Singapore, 2022, ch. 5, vol. 8.
10 M. Zubair, M. M. Ul Hassan, M. T. Mehran, M. M. Baig, S. Hussain and F. Shahzad, *Int. J. Hydrogen Energy*, 2022, **47**, 2794–2818.
11 B. He, F. Bai, P. Jain and T. Li, *Small*, 2025, **21**, 2411479.
12 Y. Luo, X. Li, X. Cai, X. Zou, F. Kang, H.-M. Cheng and B. Liu, *ACS Nano*, 2018, **12**, 4565–4573.
13 K. B. Ibrahim, T. A. Shifa, M. Bordin, E. Moretti, H.-L. Wu and A. Vomiero, *Small Methods*, 2023, **7**, 202300348.
14 Y. Pu, M. J. Lawrence, V. Celorrio, Q. Wang, M. Gu, Z. Sun, L. A. Jácome, A. E. Russell, L. Huang and P. Rodriguez, *J. Mater. Chem. A*, 2020, **8**, 13340–13349.
15 C. Tang, H.-S. Wang, H.-F. Wang, Q. Zhang, G.-L. Tian, J.-Q. Nie and F. Wei, *Adv. Mater.*, 2015, **27**, 4516–4522.
16 J. Sanchez, M. Burke Stevens, A. R. Young, A. Gallo, M. Zhao, Y. Liu, M. V. Ramos-Garcés, M. Ben-Naim, J. L. Colón, R. Sinclair, L. A. King, M. Bajdich and T. F. Jaramillo, *Adv. Energy Mater.*, 2021, **11**, 2003545.
17 M. V. Ramos-Garcés and J. L. Colón, *Nanomaterials*, 2020, **10**, 822.
18 M. V. Ramos-Garcés, J. Sanchez, D. E. Del Toro-Pedrosa, I. B. Alvarez, Y. Wu, E. Valle, D. Villagrán, T. F. Jaramillo and J. L. Colón, *ACS Appl. Energy Mater.*, 2019, **2**, 3561–3567.
19 M. V. Ramos-Garcés, J. Sanchez, K. La Luz-Rivera, D. E. Del Toro-Pedrosa, T. F. Jaramillo and J. L. Colón, *Dalton Trans.*, 2020, **49**, 3892–3900.
20 R. Vivani, F. Costantino and M. Taddei, in *Metal Phosphonate Chemistry*, ed. A. Clearfield and K. D. Demadis, Royal Society of Chemistry, London, 2011, pp. 45–86.
21 A. Donnadio, M. Nocchetti, F. Costantino, M. Taddei, M. Casciola, F. da Silva Lisboa and R. Vivani, *Inorg. Chem.*, 2014, **53**, 13220–13226.
22 M. Nocchetti, A. Donnadio, E. Vischini, T. Posati, C. Albonetti, D. Campoccia, C. R. Arciola, S. Ravaioli, V. Mariani, L. Montanaro and R. Vivani, *Inorg. Chem.*, 2022, **61**, 2251–2264.
23 F. Costantino, R. Vivani, M. Bastianini, L. Ortolani, O. Piermatti, M. Nocchetti and L. Vaccaro, *Chem. Commun.*, 2015, **51**, 15990–15993.
24 V. Kozell, T. Giannoni, M. Nocchetti, R. Vivani, O. Piermatti and L. Vaccaro, *Catalysts*, 2017, **7**, 186.
25 F. Costantino, M. Nocchetti, M. Bastianini, A. Lavacchi, M. Caporali and F. Liguori, *ACS Appl. Nano Mater.*, 2018, **1**, 1750–1757.
26 M. Nocchetti, A. Donnadio, E. Vischini, T. Posati, S. Ravaioli, C. R. Arciola, D. Campoccia and R. Vivani, *Materials*, 2019, **12**, 3185.
27 K. Moedritzer and R. R. Irani, *J. Org. Chem.*, 1966, **31**, 1603–1607.
28 C. C. L. McCrory, S. Jung, J. C. Peters and T. F. Jaramillo, *J. Am. Chem. Soc.*, 2013, **135**, 16977–16987.
29 Y. Q. Gao, X. Y. Liu and G. W. Yang, *Nanoscale*, 2016, **8**, 5015–5023.
30 G. Alberti, R. Bertrami and U. Costantino, *J. Inorg. Nucl. Chem.*, 1976, **38**, 1729–1732.
31 J. F. Moulder, W. F. Stickle, P. E. Sobol and K. D. Bomben, *Handbook of X-Ray Photoelectron Spectroscopy*, ed. J. Chastain and R. C. King Jr, Physical Electronics Division, Perkin-Elmer Corp, 1995.
32 M. Descostes, F. Mercier, N. Thromat, C. Beaucaire and M. Gautier-Soyer, *Appl. Surf. Sci.*, 2000, **165**, 288–302.
33 E. Fabbri, A. Habereder, K. Waltar, R. Kötz and T. J. Schmidt, *Catal. Sci. Technol.*, 2014, **4**, 3800–3821.
34 M. S. Burke, M. G. Kast, L. Trotochaud, A. M. Smith and S. W. Boettcher, *J. Am. Chem. Soc.*, 2015, **137**, 3638–3648.
35 M. W. Louie and A. T. Bell, *J. Am. Chem. Soc.*, 2013, **135**, 12329–12337.
36 S. Anantharaj, P. E. Karthik and S. Noda, *Angew. Chem., Int. Ed.*, 2021, **60**, 23051–23067.
37 M. Schulze, R. Reissner, M. Lorenz, U. Radke and W. Schnurnberge, *Electrochim. Acta*, 1999, **44**, 3969–3976.

